Additively Manufactured Semipassive Rotman Lens-Based RIS-Assisted mmID Tag System for Beyond-5G Wireless Networks in Complex Environments

I-Ting Chen, *Student Member, IEEE*, Charles A. Lynch III, *Student Member, IEEE*, Aline Eid, *Member, IEEE*, Jimmy G. D. Hester, *Member, IEEE*, Kai Zeng, *Member, IEEE*, and Manos M. Tentzeris, *Fellow, IEEE*

***Abstract*— The authors present a semipassive Rotman lens-based reconfigurable intelligent surface at 28 GHz for beyond-5G applications. One proof-of-concept prototype is inkjet-printed on a thin Rogers substrate using a masking technique followed by etching. The system is characterized by its autonomous mode switching, power consumption, radar cross section (RCS) against angle, and mid-range performance. This millimeter-wave identification (mmID) tag system detects radio frequency (RF) signals with a half-wave rectifier and retransmits signals in selective directions with a 270-kHz amplitude shift keying modulation. This proposed system consumes 65 μW in the detection mode and 143 μW in the communication mode, suggesting the potential to be further developed into a fully passive and energy-autonomous system for long-range applications in complex environments. To switch between detection and communication modes, the rectifier oscillates between 6.1 and 9.7 mV, which means that the Rotman lens-based RIS-assisted mmID tag system can operate up to 75 m away for communication mode and 89 m for the detection mode.**

***Index Terms*— Reconfigurable intelligence surface (RIS), Rotman lens.**

I. Introduction

THE wide deployment of 5G and millimeter-wave (mm-Wave) wireless communication technologies has made Internet-of-Things (IoT) applications possible with high data rates, low latency, high signal directivity, and high power density. The world is projected to have more than 29 billion connected devices by 2050 for IoT applications [1]. However, numerous challenges remain in adapting the mm-Wave devices to the changes in real-world environments, especially for 5G and beyond 5G frequencies. More specifically, mm-Wave technologies suffer from signal blockages and attenuation in complex environments, such as offices, houses, and cities with multiple mobile users and physical objects, as reliable mm-Wave links typically require line-of-sight (LOS) paths between transmitters and receivers. This limitation substantially restricts mm-Wave applications in complex environments such as smart cities and Industry 4.0. Beam-forming antenna and massive multiple-input–multiple-output (MIMO) designs have been explored in academia and industry to optimize device connectivity and communication efficiency [2], [3], [4]. On the other hand, the reconfigurable intelligence surface (RIS), capable of manipulating the signal direction, has emerged as a promising solution to this limitation due to its scalability and low implementation cost [5]. Conventional RISs are constructed with an array of reflecting elements, in which each element can be individually configured in phase and amplitude to manipulate the incoming electromagnetic waves in a user-desired direction [6]. Research has proposed preliminary designs to tune the phase and amplitude of the incident wave to achieve efficient communication in a specific direction in a complex and dynamic environment with software controls, real-time monitoring, and assistance of artificial intelligence/machine learning techniques [7], [8], [9]. Additional research has further explored RIS-assisted technology to be implemented as part of 5G and even 6G communication networks [10]. However, conventional RIS and RIS-assisted technologies have several drawbacks, including high power consumption on a scale of watts and intensive computation [7], [11]. Therefore, there is a need for a low-power device that can achieve user-controllable beamforming to optimize the signal link between the transmitter and receiver at mm-Wave for the practical implementation of IoT applications.

The Rotman lens, a passive beamforming device, is proposed as a novel solution for the aforementioned drawbacks while maintaining the benefit of RIS-assisted devices.

Manuscript received 14 April 2024; revised 10 June 2024; accepted 19 June 2024. Date of publication 10 July 2024; date of current version 7 January 2025. This work was supported in part by the U.S. National Science Foundation (NSF) under Grant 2131406 and in part by the U.S. National Science Foundation Networking Technology and Systems (NeTS) Program under Grant 2131507. *(Corresponding author: I-Ting Chen.)*

I-Ting Chen, Charles A. Lynch III, and Manos M. Tentzeris are with the School of Electrical and Computer Engineering, Georgia Institute of Technology, Atlanta, GA 30332 USA (e-mail: ichen64@gatech.edu).

Aline Eid is with the Department of Electrical and Computer Engineering, University of Michigan, Ann Arbor, MI 48109 USA.

Jimmy G. D. Hester is with Atheraxon Inc., Atlanta, GA 30308 USA.

Kai Zeng is with the Department of Electrical and Computer Engineering, George Mason University, Fairfax, VA 22030 USA.

Color versions of one or more figures in this article are available at https://doi.org/10.1109/TMTT.2024.3422386.

Digital Object Identifier 10.1109/TMTT.2024.3422386

Previous research has proposed using a Rotman lens to achieve high gain with wide angular coverage for mm-Wave energy harvesting and backscattering radio frequency identification (RFID) applications [12], [13]. However, [12] presents unprogrammable beaming of the incident mm-Wave signals. A previous work in [14] presented a preliminary conceptual design of a Rotman lens-based system, demonstrating that a low-power RIS-assisted millimeter-wave identification (mmID) tag system can be possible in mid-range up to 11 m, but only individual components were characterized for different power levels without any specifics on system-level integration. However, to replace high-power consumption phased array-based devices with a Rotman lens-based design, it is essential to demonstrate a long-range operation capability while characterizing the tag performance as an integrated system. This work aims to take a step further by developing a fully autonomous and controllable beamforming device with wide angular coverage, in other words, the scannability in conventional and software-controlled RIS and RIS-assisted devices, at mm-Wave to achieve a low-power RIS-assisted mmID tag system. This work, for the first time, applies the exceptional angular scannability properties of the Rotman lens to passively achieve mm-Wave signal rebeaming in a selected direction, in contrast to consuming milliwatts to watts of power in the current RIS and RIS-assisted literature. In addition, since the power needed for detecting signals is lower than that of backscattering communication due to the capability to switch between detecting and communicating, this design is significantly more power efficient and only backscatters signals when needed.

II. Rotman Lens-Based RIS mmID System

In a complex environment, mm-Wave signals are deteriorated and blocked by objects such as buildings, vehicles, and landscape plants in an urban city. Therefore, the high data rate and low latency transmission realized by using mm-Wave face the challenge of high data rate communication only happening in LOS conditions. The Rotman lens, a fully passive true time delay architecture, presents a cheap and efficient solution for this challenge by its ability to map its port to a specific radiation direction in space, as shown in Fig. 1. When a specific port is excited, the signal selectively transmits to a specific direction. Vice versa, when an incoming signal impinges on the Rotman lens from a specific angle, the signal focalizes constructively through the lens at the respective port [15]. This work sets the system to be used in environments where IoT devices and mobile users in different port directions have no access to each other; in other words, LOS links are not available between devices in different port directions. Leveraging the unique feature of the Rotman lens, this RIS-assisted mmID tag system can receive signals from one direction, modulate the signals, and redirect the modulated signals to a different direction. This selective beamforming feature is similar to what other conventional RIS and RIS-assisted devices achieve by tuning the phase and amplitude of the impinging EM waves with significant power consumption, except this Rotman lens-based RIS-assisted mmID tag system achieves it passively. This indicates that using a Rotman lens as a RIS-assisted

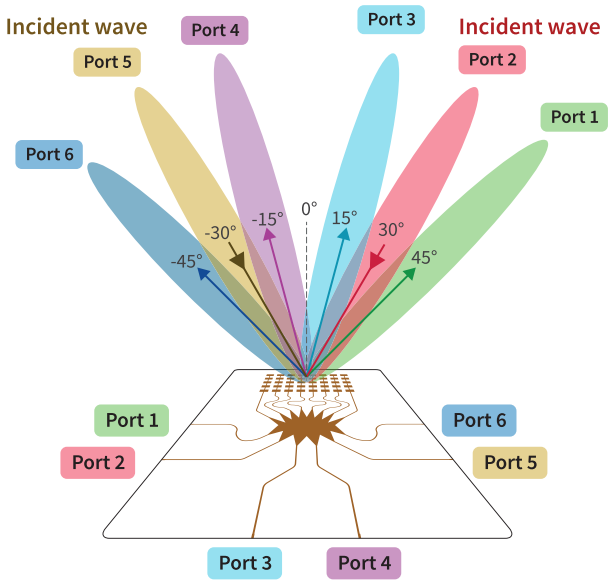

Fig. 1. Rotman lens beamforming pattern.

device significantly reduces total power consumption by using a highly energy-efficient beamforming method. In addition, low system power consumption means that this design can be made semipassive or fully passive, supplied by harvesting energy from the environment.

The proposed Rotman lens-based RIS-assisted mmID tag system can, therefore, be configured to operate in two modes: 1) detection mode and 2) communication mode. To achieve this two-mode operation, an mm-Wave detector is integrated into the system. The detection mode is enabled with a half-wave rectifier at 28 GHz, and the sensitivity is enhanced by a low-power operational amplifier (op-amp). The communication mode is accomplished by the use of a Rotman lens with 8 branches of 5×1 antenna arrays, also designed at 28 GHz. The switching of the two modes is determined by the voltage harvested and the use of eight low-power single-pole, double-throw (SPDT) nonreflective switches with a carefully designed baseband circuit that will be described in Section III. In this work, the Rotman lens and the antenna arrays are simulated and optimized in CST studio for their beamforming performance, antenna radiation pattern, and gain, while the rectifier is optimized in Keysight ADS for its power conversion efficiency on Rogers RO4350B substrate ($\epsilon_r = 3.66$ and $h = 170\ \mu$m). SPDT switches are also characterized as operating at the lowest voltage and power possible. The symmetric radiation pattern is previously presented in [14]. Fig. 1 displays the 3-D view of the radiation pattern where respective port excitation allows the signal to transmit in respective directions. Fig. 2 demonstrates how the designed Rotman lens-based RIS-assisted mmID tag system operates in a realistic environment where some none-line-of-sight (NLOS) links exist between the base stations and the mobile users. Users 1 and 4 have lost their access to base stations due to buildings blocking the signal path. User 2 has lost base station access due to the NLOS link and is outside the base station coverage. User 3 has no access to any nearby

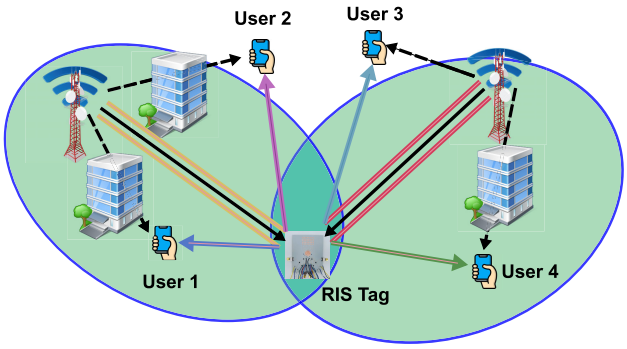

Fig. 2. Rotman lens-based RIS-assisted mmID tag system operation in a realistic environment. The black solid lines represent valid signal links, while the black dashed lines represent blocked or attenuated signal links. The colored solid lines represent how the RIS tag operates to establish valid signal links for mobile users in the environment.

base stations. The RIS tag can be placed at the intersection of the coverage of the two nearby base stations to serve multiple mobile users who lost communication access due to the signal blockage caused by the infrastructures. Since the Rotman lens-based RIS-assisted mmID tag system is symmetric, only half of the system will be described in this article, but the entire system is characterized to validate that the other half of the system performs identically.

III. Proof-of-Concept Prototype

The RF circuit of this RIS-assisted mmID tag system consisted of the well-characterized Rotman lens signal beamforming, a half-wave rectifier for RF signal detection, and eight low-power SPDT nonreflective switches, MASW-011102, from Macom for system switching. The SPDT switches control the signal beamforming and modulation, including two "Mode SPDTs" to switch between the two modes, two "Path SPDTs" to control the beam direction selection, and four "Oscillating SPDTs" to provide amplitude-shift keying (ASK) modulation at 270 kHz. This SPDT switch is a dual control switch requiring a ground voltage and a minimum negative voltage.

The baseband circuit is designed to control the RF SPDT switches (Mode SPDTs, Path SPDTs, and Oscillating SPDTs). This baseband circuit connects the rectifier to a 470-μF charging capacitor and to an MCP6042 rail-to-rail op-amp from Microchip Technology. The op-amp is then connected to a four-channel SN74HCS125 quadruple Schmitt trigger from Texas Instruments, followed by two MAX868 inverters from Analog Devices (inverters 1 and 2) and a low-power TS3006 Semi Oscillator from Touchstone Semiconductor. The SN74HCS125 contains four independent channels with three-state outputs and Schmitt-trigger inputs. Each channel performs the Boolean function $Y = A$ in positive logic. The outputs can be put into a Hi-Z state by applying a digital High on the channel-corresponding enable (OE) pin. Only two channels, channel 3 and channel 4, are used. Each channel is independent and has to be enabled by connecting its OE pin to a digital LOW voltage bias, which is ground in this design. In addition, a 1.5-V solar cell is connected to a third MAX868 inverter (inverter 3), which is connected to

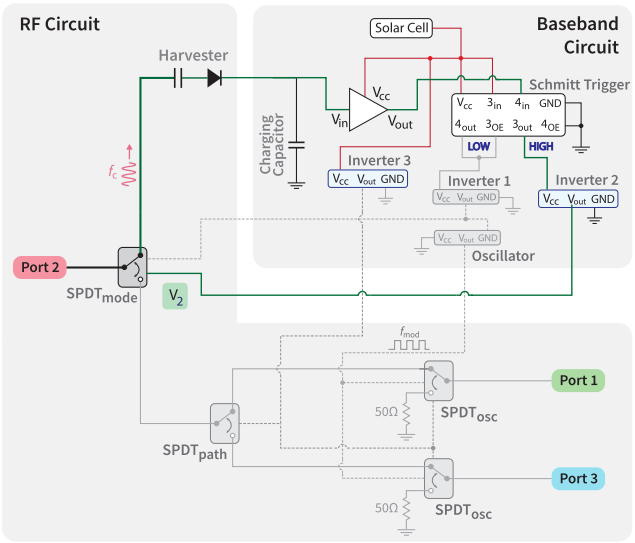

Fig. 3. Rotman lens-based RIS-assisted mmID tag system schematic in detection and harvesting mode.

the voltage biasing of the Path SPDTs on the RIS-assisted mmID tag system, also controlled by mechanical switches. The detailed construction of the baseband circuit is shown in Figs. 3 and 4. By connecting the supply voltage pin on the oscillator to the ground, this can output a negative voltage swing at 270 kHz for ASK modulation. This modulation frequency is chosen mainly due to the capability of the oscillator. It is critical to select a low-power oscillator that is capable of operating negative voltage swings. Therefore, the TS3006 Semi Oscillator is chosen for this design. The phase noise generated from the signal generator is calculated by $\mathcal{L}(f) = 1.877 \times (\Delta f)^{0.2707} - 48.19$, where $\mathcal{L}(f)$ is the phase noise in dBc/Hz at Δf away from the carrier. It is expected that the higher the modulation frequency is, the higher the power consumption from the oscillator, while the higher the signal-to-noise ratio (SNR). Therefore, the modulation frequency 270 kHz from this oscillator is chosen to maintain low power consumption while overcoming the phase noise at -103.9 dBc/Hz.

The RIS-assisted mmID tag system first operates in the detection mode, detecting and rectifying mm-Wave signal at 28 GHz in the environment. Fig. 3 displays the system schematic in the detection mode, where the grayed-out components are inactive. Incident waves are focalized through the Rotman lens into Port 2 and detected by the half-wave rectifier designed with a Macom MA4E1317 Schottky diode. A 100-nF 560L104YTRN capacitor from Mouser is used as a dc block to prevent the harvested dc voltage from flowing back to the SPDTs and damaging the components. The rectifier design and its characterization are previously presented in [14]. When the RIS-assisted mmID tag system is first in the detection mode, the rectifier charges up the capacitor, accumulating dc voltage. While the dc voltage builds up, the op-amp outputs a low voltage into the channel 4 input pin (4in) on the Schmitt trigger, generating a digital LOW output voltage. This digital LOW voltage is connected to channel 3 enable pin (3OE), enabling channel 3. Since the channel 3 input pin (3in) is

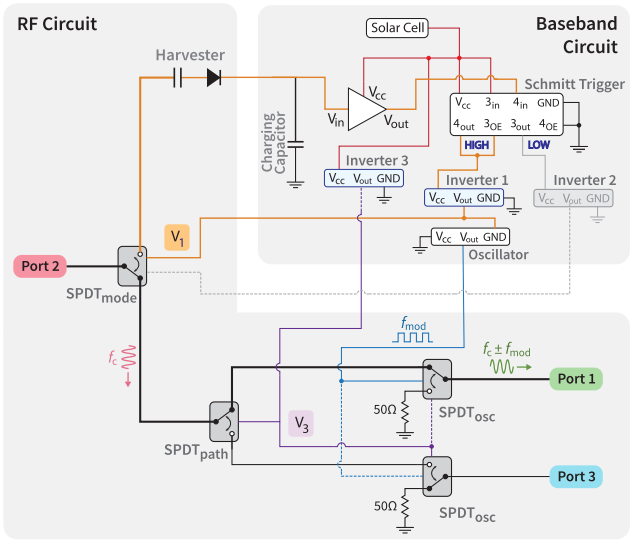

Fig. 4. Rotman lens-based RIS-assisted mmID tag system schematic in the communication mode.

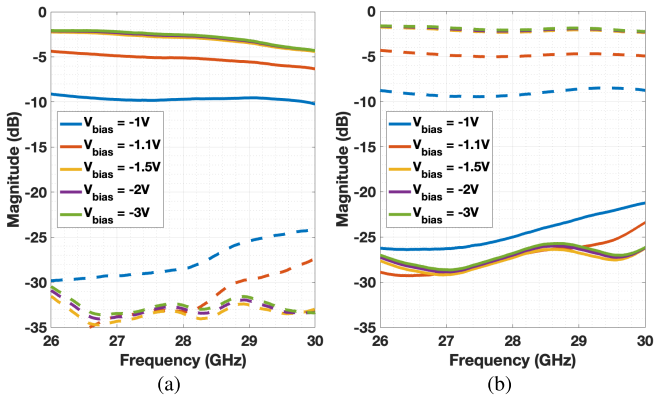

Fig. 5. MASW-011102 biasing voltage characterization when configured for signal transmission for (a) Path 1 and (b) Path 2. The solid lines represent deembedded S_{21}, and the dotted lines represent deembedded S_{31}.

supplied by a solar cell, the channel 3 output pin (3out) outputs a digital HIGH voltage that is connected to inverter 2. When inverter 2 is on, the Mode SPDT is controlled to be in the detection mode.

When the voltage on the storing capacitor builds up and allows the op-amp to output a voltage that reaches the high voltage threshold into the channel 4 input pin (4in), channel 4 outputs a digital HIGH voltage, switching the RIS-assisted mmID tag system from detection mode into the communication mode, as shown in Fig. 4. The digital HIGH voltage from the channel 4 output pin (4out) is fed into the channel 3 enable pin (3OE), disabling channel 3 and turning off inverter 2. On the other hand, channel 4 digital HIGH voltage is fed into inverter 1, connected to the low power oscillator, and another voltage biasing on the Mode SPDTs, controlling the system to be switched to communication mode. Since the supply voltage pin of the oscillator is grounded, the oscillator generates a 270-kHz negative oscillation that is fed into the Oscillating SPDTs, creating an ASK at 270-kHz. As the RIS-assisted mmID tag system operates in the communication mode, the charging capacitor discharges its voltage. When the capacitor discharges to the low voltage threshold, the RIS-assisted mmID tag system switches back to the detection mode and builds up the voltage again.

During both detection and communication modes, the unused ports on the Rotman lens are terminated at 50 Ω to reduce the radiation sidelobe and improve port isolation. This is achieved by connecting a solar cell to supply a third inverter (inverter 3) that feeds into the Path SPDTs and Oscillating SPDTs, which are controlled by mechanical switches for simplicity. In further designs, this third inverter and mechanical switches can be eliminated by combining them into the Schmitt trigger, inverter 1, and inverter 2.

Before implementation into the system, the SPDT switch is characterized to obtain the minimum biasing voltage needed. The microstrip lines are simulated in CST studio on the same Rogers RO4350B substrate for impedance matching and connected to the SPDT. This experiment is done by supplying different biasing voltages to the SPDT and monitors the 28-GHz RF signal transmission with a ShockLine MS46522B vector network analyzer (VNA) from Anritsu. It can be seen in Fig. 5 that the magnitude of the signal transmission stays consistent when the biasing voltage is less than −1.5 V. Therefore, a negative voltage biasing of −1.5 V is considered the operating threshold for experiments in Section IV for the Rotman lens-based RIS-assisted mmID tag system evaluation.

The RIS-assisted mmID tag system is fabricated on Rogers RO4350B substrate ($\epsilon_r = 3.66$ and $h = 170$ μm) using an inkjet printing technique. A masking SU8 layer generates the pattern, followed by an etching process. The fabricated design prototype is shown in Fig. 6 and is set up as shown in Fig. 7 for characterization. The baseband is constructed on a through-hole breadboard, and an MP3-25 from PowerFilm, Inc., is used. Due to the low power needed for the system, only half of the solar cell is used. The solar cell, 114 × 24 mm in size, supplies 1.5 V to the RIS-assisted mmID tag system to both the RF and baseband components. The system is evaluated in four aspects, presented in Section IV, with the setup kept identical, as shown in Fig. 7.

IV. Evaluation of Rotman Lens-Based RIS mmID System

Since this RIS-assisted mmID tag system aims to assist future 5G and beyond wireless networks, it is essential to evaluate its performance in the far-field. To place the transmitting and receiving antennas in the far-field of the RIS-assisted mmID tag system, the distance between the antennas and the system has to be greater than $(2D/\lambda)$, where D represents the diameter of the antenna. Two horn antennas with 20-dBi gain from A-Info are used in the experiments as the transmitting and receiving antennas. Considering the horn antenna size and the patch antenna size on the RIS-assisted mmID tag system, far-field experiments will be done by placing the transmitting and receiving antennas at least 0.4 m away from the system. In this section, experiments are done independently and separately. Therefore, the distance varies from 1.3 to 2 m

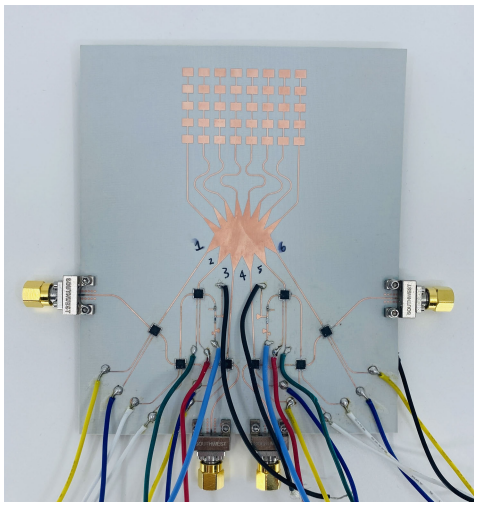

Fig. 6. Rotman lens-based RIS-assisted mmID tag system with a size of 12 cm × 11 cm.

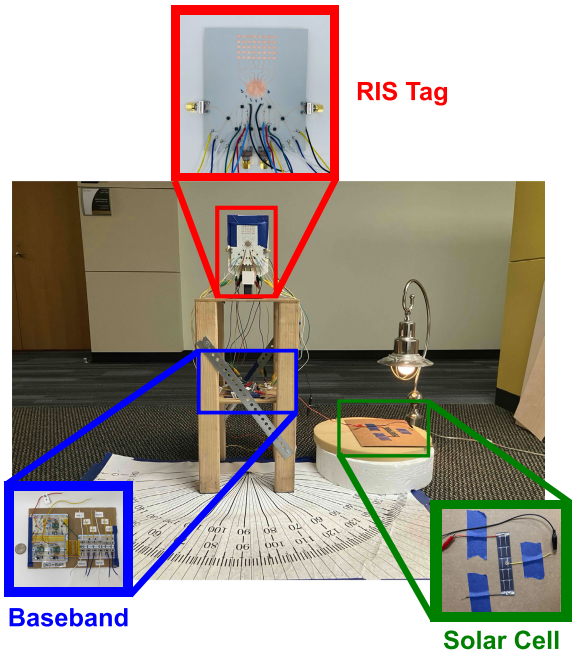

Fig. 7. Rotman lens-based RIS-assisted mmID tag system measurement setup including the RIS tag, baseband, and solar cell labeled.

for short-range characterization due to the physical limitation of the testing space.

A. Baseband Circuit Voltage Swing Analysis

This measurement is done by placing two horn antennas with 20-dBi gain from A-Info in a bi-static form at 2 m away from the RIS-assisted mmID tag. An 83640L Signal Generator from Agilent is used to generate a continuous wave (CW) 28 GHz to the transmitting antenna, sending 52-dBm EIRP to the RIS-assisted mmID tag system. The receiving antenna is connected to an FSW43 signal and spectrum analyzer from Rohde & Schwarz to monitor the presence of signal modulation when in the communication mode. The three negative voltages ($V1$, $V2$, and $V3$ labeled in Figs. 3 and 4) are monitored with digital multimeters, sampling at every

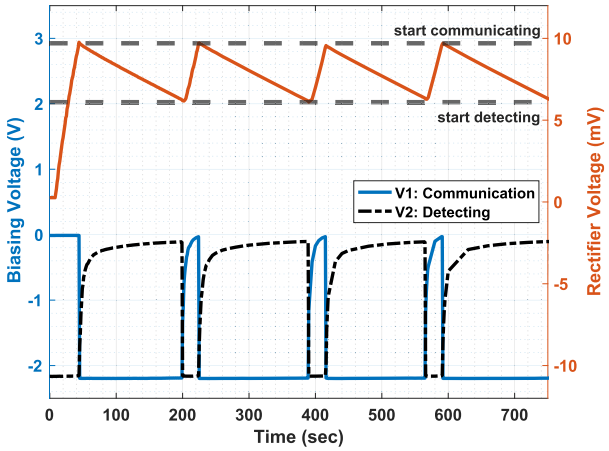

Fig. 8. Baseband voltage swing versus time displaying the rectifier output in the red solid trace, biasing voltage for communication in the blue solid trace, and biasing voltage for detection in the black dashed trace.

second. The threshold voltage is based on the Schmitt trigger configuration and confirmed in measurements shown in Fig. 8 that the high voltage threshold for the RIS-assisted mmID tag system to start communicating is 9.7 mV and the low voltage threshold for the system to switch back to detection is 6.1 mV. The op-amp has a gain of 85 for a tradeoff between power consumption and operation range, which will be discussed more in Section IV-B. When the harvester builds up the voltage on the storing capacitor to 9.7 mV, the op-amp outputs 893 mV into the Schmitt trigger, switching the system into the communication mode. When the storage capacitor discharges the voltage to 6.1 mV, the op-amp outputs 536 mV into the Schmitt trigger, switching the system back to the detection mode.

$V1$ and $V2$ in Fig. 8 represent the negative voltage biasing shown in Figs. 3 and 4. When $V1$ is less than -1.5 V, the RIS tag system operates in the communication mode. When $V2$ is less than -1.5 V, the RIS tag system operates in the detection mode. The red label represents the rectifier voltage before feeding into the op-amp. It can be seen in Fig. 8 that voltage biasing quickly restores when the system switches between two modes. The duty cycle for communication mode is 86.3%.

B. Power Consumption and Link Budget Analysis

This measurement is taken with the same setting as Section IV-A. In addition, the current at the solar cell is monitored with a digital multimeter, sampling at every second. The power consumption is then calculated and shown in Fig. 9 when the RIS-assisted mmID tag system operates in different modes. The blue represents the rectifier voltage before feeding into the op-amp, while the red represents the power consumption at different modes. It can be seen that the system consumes 65 μW when operating in the detection mode for the op-amp, Schmitt trigger, and inverter 2 and consumes 143 μW when operating in the communication mode for the op-amp, Schmitt trigger, inverter 1, and oscillator. It is important to analyze how much power the system consumes in two different modes to evaluate whether this design is suitable to

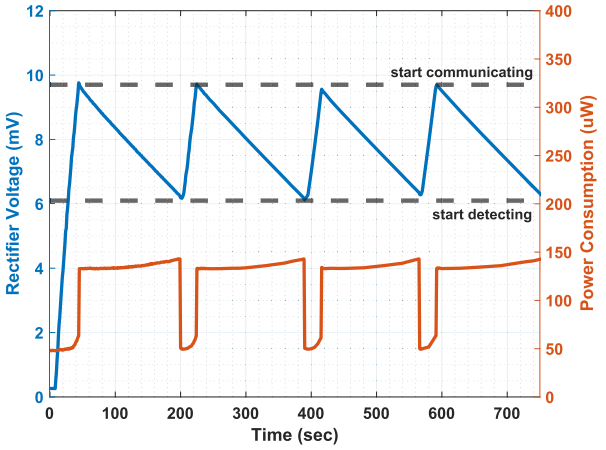

Fig. 9. Rotman lens-based RIS-assisted mmID tag system power consumption analysis.

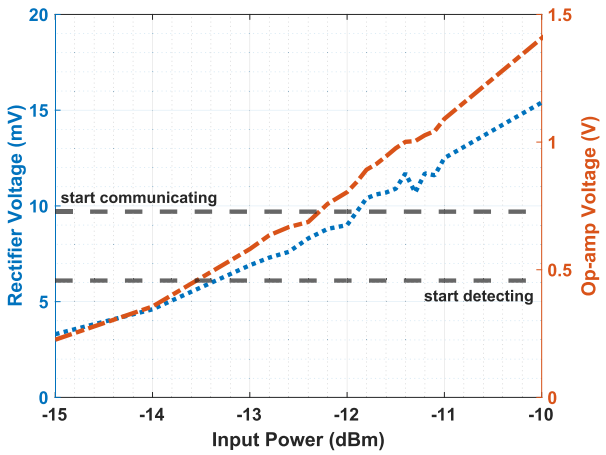

Fig. 10. Half-wave rectifier voltage characterization with op-amp.

be implemented for IoT applications, where replacing batteries for each sensor and device is not feasible. Since the system consumes low energy, it is currently supplied by a single solar cell and has the potential to be implemented in future IoT applications by replacing the solar cell with an efficient mm-Wave signal harvester.

Fig. 10 shows the input power in dBm versus the rectifier voltage and the voltage at the op-amp output. It can be seen that the op-amp has a gain of 85, and the rectifier can be turned on at a very low input power at −15 dBm. In order to reach the voltage threshold for communication, the rectifier has to output 9.7 mV at −11.9 dBm. For the RIS-assisted mmID tag system to switch back to the detection mode, the rectifier has to stay above 6.1 mV at −13.4 dBm. According to the Federal Communications Commission (FCC), the allowed effective isotropic radiated power (EIRP) at 28 GHz is 75 dBm. The furthest distance of operation is calculated by

$$P_{\text{tag}} = P_{\text{Tx}} - L_{\text{fs}} + G_{\text{tag}} \tag{1}$$

where P_{tag}, P_{Tx}, L_{fs}, and G_{tag} represent the power received by the RIS mmID tag system in dBm, the EIRP of the transmitter in dBm, free space loss dB, and the gain of the RIS mmID tag system in dBi. Considering the average gain of the Rotman lens G_{tag} to be 12 dBi, when in the detection mode, the minimum impinging power P_{tag} sent into the rectifier has to reach −13.4 dBm. With 75-dBm EIRP and considering the free path loss calculated by

$$L_{\text{fs}} = 20 \times \log\left(\frac{4\pi R}{\lambda}\right) \tag{2}$$

where L_{fs}, R, and λ represent free space loss dB, distance the signal travels in meters, and free space wavelength at 28 GHz in meters, this RIS-assisted mmID tag system can operate up to 89 m for the detection mode. Similarly, the minimum inspiring power P_{tag} sent to the rectifier has to reach −11.9 dBm for the system to switch into the communication mode. Based on the free space loss calculated at 28 GHz, this RIS-assisted mmID tag system can operate up to 75 m away for communication mode.

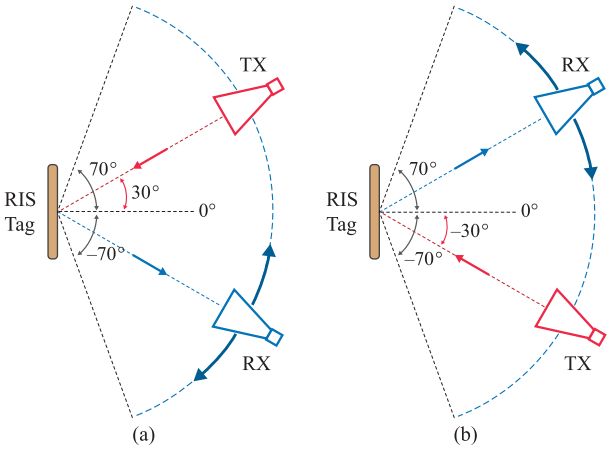

Fig. 11. Rotman lens-based RIS-assisted mmID tag system angular sweep setup where the red transmitting antenna (a) placed at Port 2 at 30° and (b) placed at Port 5 at −30° while the blue receiving antenna scanning from −70° to 70°.

C. Time Delay and RCS Analysis

This measurement is done by placing two same horn antennas from Section IV-B in a bi-static form at 1.3 m away from the RIS-assisted mmID tag, as shown in Fig. 11(a). The transmitting antenna is set to locate at 30° (Port 2) from normal, while the baseband circuit is configured to rebeam the signal to either 15° (Port 1) or 45° (Port 3). The receiving antenna is then swept from −65° to 65° for signal monitoring. This measurement is repeated for the other half of the RIS-assisted mmID tag, as shown in Fig. 11(b). The transmitting antenna is placed in −30° (Port 5), while the baseband circuit is configured to redirect signals in either −15° (Port 4) or −45° (Port 6). Only half of the RIS-assisted mmID tag will be discussed [Measurement Setup (a)] as the system is designed to be symmetric.

Both the transmitting and receiving antennas are connected to a ShockLine MS46522B VNA from Anritsu for data collection from 20 to 35 GHz with an intermediate bandwidth of 300 Hz. The two states, ASK modulation ON and OFF, are configured when taking S-parameter measurements. When in the ON state, the oscillating SPDT is biased with a constant −1.5 V, allowing the signal to redirect to a user-chosen

TABLE I
T_d FOR ON AND OFF STATES OF RIS-ASSISTED MMID TAG SYSTEM

State	SPDT	Transmission Line
ON	3	77.224 mm
OFF	4	95.06 mm

direction. When in the OFF state, the oscillating SPDT is grounded, making the signal reflect back retrodirectively. The OFF state data are then subtracted from the ON state data before applying the inverse Fourier transform and time gating to obtain the differential time-domain response. The time gating window is calculated by the time spent between the delivery of the RF signal from the transmitting antenna and the receipt of the rebeam signal at the receiving antenna. It is noted that the conventional time gating window is calculated by expecting the impinging RF signals to reflect from the tag immediately, meaning that the time delay that the signal spent traveling inside the tag substrate transmission lines (T_d in Fig. 12) is 0, and therefore, the total travel time is calculated by two times of the distance between the antenna and the system divided by the speed of light. However, due to the mechanism of beam redirection of this design, RF signals travel additional time ($T_d \neq 0$) through the additional SPDTs and microstrip lines on the system at a speed less than the speed of light before retransmitting the RF signal to a desired direction. To confirm this, a measurement is set up with one SPDT with two legs of antenna arrays, as shown in the upper left corner of Fig. 13. The two same horn antennas used in Sections IV-A and IV-B are colocated with perpendicular polarization at 0.95 m away from the testing structure. The time-domain response is analyzed to characterize T_d of each SPDT. The speed at which the RF signal travels in the system substrate is characterized by Rogers in its Microwave Impedance Calculator according to the height and the dielectric constant of the substrate, and the extra time delay from one SPDT is characterized in Fig. 13. Considering the RF travel speed in RO4350B to be 1.7×10^8 m/s and the travel time within the SPDTs and microstrip line, the total time of travel is calculated by

$$T_{\text{total}} = 2 \times \text{ToF} + T_d \tag{3}$$

where ToF, time of flight, is the physical distance between the device and the transmitter and receiver divided by the speed of light and T_d is the time the signal travels in the device. For the ON state, the signal travels once through the Mode SPDT, Path SPDT, and Oscillating SPDT. For the OFF state, the signal travels twice through the Mode SPDT and Path SPDT. Therefore, the travel time in the substrate, T_d, is different for ON and OFF states. Table I shows the number of SPDTs and the length of the transmission line for each state. Since differential radar cross section (RCS) is being evaluated, the average of SPDTs and transmission line length is used to estimate the expected T_d.

From Fig. 14, it can be seen that there are two differential responses at 9 and 11.375 ns. Since the RIS-assisted mmID tag system is placed at 1.3 m away from the receiver and the transmitter, the response at 9 ns is the reflective response from the ground plane, and therefore, the 11.375 ns response is the

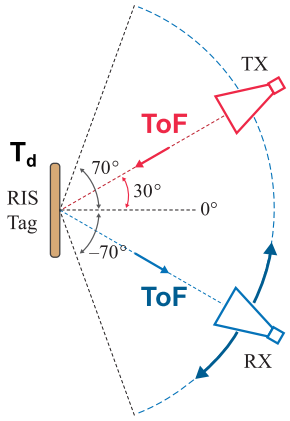

Fig. 12. Rotman lens-based RIS-assisted mmID tag system RCS and time delay measurement setup.

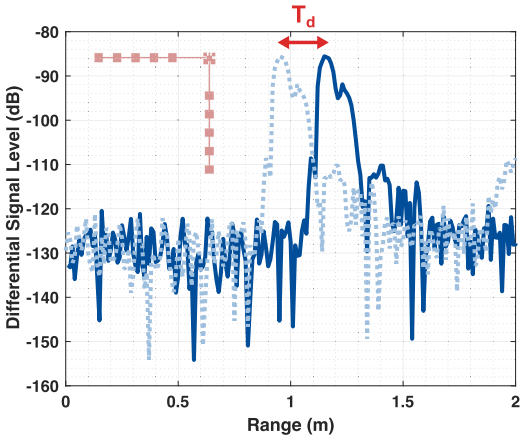

Fig. 13. SPDT switch time-domain response when placing 0.95 m away from the transmitting antenna, where the dotted line represents where the response is expected to show when $T_d = 0$ and the solid line represents the actual response.

differential modulated tag response. Considering the average SPDT as $((3 + 4)/2) = 3.5$ and the average transmission line length as $((77.224 + 95.06)/2) = 86.142$ mm, a formula can be written as

$$\frac{1.3 \times 2 + 0.086142 + 3.5 \times \text{SPDT}_{\text{disp}}}{c} = 11.375 \text{ ns} \tag{4}$$

where c represents the speed of light and $\text{SPDT}_{\text{disp}}$ is the displacement of a single SPDT. It is calculated that $\text{SPDT}_{\text{disp}} = 0.206$ m. To validate this calculation, an additional measurement is done to characterize the T_d for one single SPDT by connecting one SPDT switch to two branches of antenna arrays to measure the delay between the two cross-polarized signals. It can be seen that when the SPDT is placed at 0.95 m away, the differential signal response shows up at 1.15 m instead. This shows that each SPDT contributes to 0.2 m of displacement, consistent with the aforementioned calculation.

The time gating window is then adjusted by using

$$T_{\text{gating}} = \frac{T_{\text{total}}}{2 \times c} \tag{5}$$

where c is the speed of light. T_{gating} is calculated to be set at 1.705 m even though the tag system is physically placed at 1.3 m away. After adjusting the time gating window with

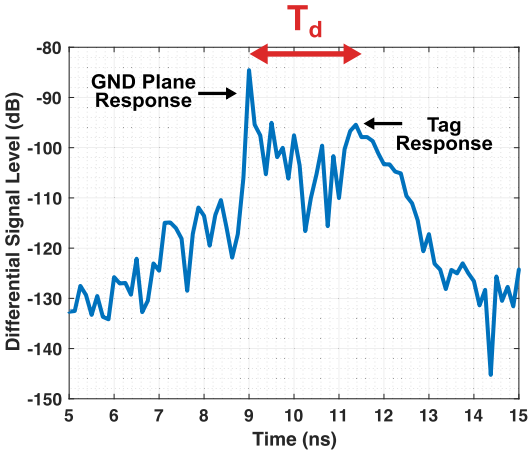

Fig. 14. Rotman lens-based RIS-assisted mmID tag system differential time-domain response when placing at 1.3 m away from the transmitter and receiver.

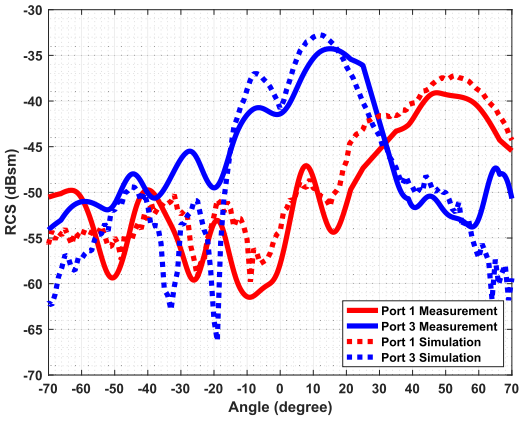

Fig. 15. Rotman lens-based RIS-assisted mmID tag system RCS against sweeping angles.

the additional time delay, the differential RCS is then adjusted according to a measured RCS from a metal ball with 30.48 cm (12 in) in diameter. The reference RCS is calculated by $\mathrm{RCS}_{\mathrm{ref}} = \pi r^2$, where r is the radius of the metal ball in meters. It is shown in Fig. 15 that the RIS-assisted mmID tag system RCS changes along with the sweeping angle. When the baseband is configured to redirect signals from Port 2 to Port 1, the maximum RCS appears in the rebeaming direction at 15°. When the baseband is configured to redirect signals from Port 2 to Port 3, the maximum RCS appears in the rebeaming direction at 45°. The simulated differential RCS is calculated using

$$\Delta_{\mathrm{RCS}} = \frac{\lambda^2 G_{\mathrm{receive}} G_{\mathrm{retransmit}} |\Gamma_{\mathrm{ON}} - \Gamma_{\mathrm{OFF}}|^2}{4\pi} \tag{6}$$

where λ, G_{receive}, $G_{\mathrm{retransmit}}$, Γ_{ON}, and Γ_0 represent the free space wavelength of operation in meters, the gain of the Rotman lens receiving port and redirecting port in dBi, and the reflection coefficient in ON and OFF states, respectively. In conventional retrodirective mmID designs, $G_{\mathrm{receive}} = G_{\mathrm{retransmit}}$. However, in this article, since signals are redirected to a different direction than the incoming direction by different port excitation, the gain roll-off at the Rotman lens outside the port needs to be considered. In this evaluation, the receiving port is set to port 2 on the Roman lens, and the retransmitting port is set to be either port 1 or port 3, controlled by the baseband configuration. The evaluation also considers the extra transmission line loss on the physical design. In Fig. 15, it is shown that the measured RCS pattern corresponds to the simulated RCS. This result highlights the selective beaming capability of the design. It is also shown that the Port 1 peak RCS is 5 dB lower than the peak RCS at Port 3. This is mainly due to the gain roll-off of the Rotman lens. It is estimated that the most outer ports of the Rotman lens have a gain that is 2–3 dB lower compared to the middle ports. Since RCS measurement is taken by estimating the redirecting signal from the RIS-assisted mmID tag system, the two-way link creates a 5–6-dBm difference in differential RCS.

D. Indoor Mid-Range Analysis

The Rotman lens-based RIS-assisted mmID tag system is finally evaluated at indoor mid-range from 2 to 13 m away with the bistatic configuration of the transmitting and receiving horn antennas, while the tag is in the communication mode to validate the long-range possibility with the set up shown in Fig. 16. The same measurement setup as Section IV-C is used for this measurement with the 43.1-dBm EIRP from the transmitting antenna. The transmitting antenna is placed at an angle of incidence of 30° to normal at Port 2, and the power level of the 270-kHz subcarrier is monitored and recorded 15° at Port 1 and at 45° at Port 3, respectively, with proper baseband circuitry configuration, using an FSW43 signal and spectrum analyzer from Rohde & Schwarz. While the measured power level decreases with the distance increasing, the phase noise also decreases. Because this RIS-assisted mmID tag system is specifically designed for applications that place transmitting and receiving antennas in a bistatic form, it is expected that the receiving signal is less affected by phase noise, like the previous research where the transmitting and receiving antennas are colocated. Fig. 17 shows that the SNR decreases with distance increasing, mainly due to the path loss. The SNR results are taken at port 1 and port 3 with their corresponding baseband configuration. It can be seen that port 1 SNR is slightly lower than port 3 SNR, mainly due to the outside port gain roll-off from the Rotman lens. The SNR is still able to maintain greater than 20 dB when the transmitting and receiving antennas are 13 m away from the RIS-assisted mmID tag system. In addition, with the increased allowed EIRP at mm-Wave, this design has the potential to be used in long-range communication networks when the transmitter and receiver are not colocated.

Table II compares this proposed design with existing RIS-assisted prototypes. It can be seen that the other existing designs achieve signal redirection with more freedom to elevation and azimuth angles with the cost of more power consumption from the use of phased arrays and software-defined radio (SDR). The system power consumption of the proposed design is significantly lower due to the use of the Rotman lens. It is also noted that [7] is the only design that operates at mm-Wave, but only simulated results were presented.

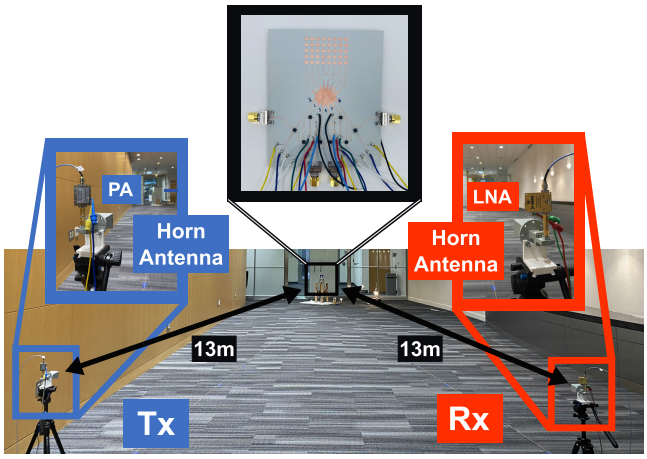

Fig. 16. Rotman lens-based RIS-assisted mmID tag system indoor mid-range measurement setup.

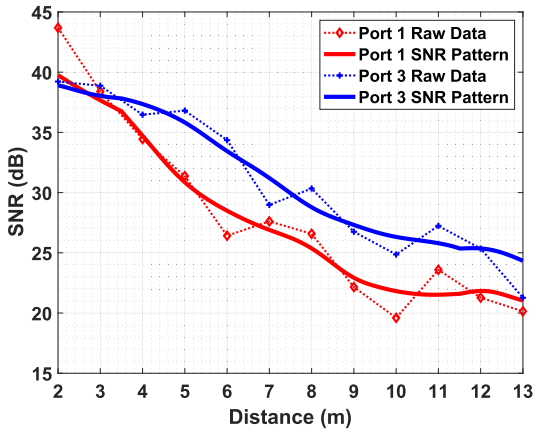

Fig. 17. Rotman lens-based RIS-assisted mmID tag system indoor mid-range SNR against distance.

TABLE II
STATE-OF-THE-ART COMPARISON OF RIS DESIGNS

Ref.	[7]	[8]	[11]	This work
Freq.	60 GHz	5.2 GHz	4.25 GHz	28 GHz
Beamforming Method	Phased Arrays / SDR			Rotman Lens
Power Consumption	1.88 W	N/A	0.72 W	65 µW / 143 µW
Re-direction Coverage	Elevation Azimuth	Azimuth	Elevation Azimuth	Azimuth

V. CONCLUSION

This work demonstrates a low-power Rotman lens-based RIS-assisted mmID tag system that can be operated in two modes at the 5G mm-Wave frequency band. This proof-of-concept design presents an alternative to the conventional RIS and RIS-assisted devices that are power-hungry and computationally heavy. In addition, with its low power consumption, 65 μW in the detection mode, and 143 μW in the communication mode, it is expected that this Rotman lens-based RIS-assisted mmID tag system has the potential to be further developed to a fully passive device supported by wireless energy harvesting. In addition, operating the system in the more power-hungry beam redirection (communication) mode only when needed allows the system to operate more efficiently and, therefore, last longer. With the detection mode, the system can intermittently check if the signal source is still present before switching to communication mode, which causes more power. To switch between detection and communication modes, the detector oscillates between 6.1 and 9.7 mV. With 75-dBm EIRP, this RIS-assisted mmID tag system can operate up to 75 m away for communication mode and 89 m for the detection mode. Meanwhile, since the use case for this system assumes that the transmitting and receiving antennas are spatially separated in the bistatic configuration, the RCS and indoor mid-range analysis also suggest that this system can be operated in long-range with high sensitivity while being copolarized to enhance wireless communication networks in complex environments with controllable and selective beamforming. Meanwhile, due to the long transmission line on the device to enable redirecting capability, the redirecting signal travels to the receiver slower than the reflective signal from the ground plane. Even though the length of the transmission lines is on a mm scale, it is significant enough to be easily distinguishable in the time domain, simplifying the calibration in signal processing. It is important to note that this preliminary design is a static proof of concept in which the redirecting direction is restricted. A multilayer design to avoid RF signal crossovers with an increased number of ports of the Rotman lens can increase the beamforming selectivity to receive and redirect signals from and to any direction. In addition, an N-by-N scalable structure can be built using this design as the unit element. Because of the use of the Rotman lens, each element in an N-by-N structure can still function as a single RIS device. Therefore, the N-by-N structure can serve as a single RIS collectively for single-direction beaming or multiple RISs for multiple-direction beaming simultaneously. Since most existing RIS and RIS-assisted devices are realized using phased arrays that consume significant power, it is not feasible to develop them into energy-autonomous designs using RF energy harvesting techniques. This work, on the other hand, displays a Rotman lens-based RIS-assisted mmID tag system that maintains the functionality of a traditional RIS with low power consumption, making an energy-autonomous RIS development possible. It presents the potential for fully passive beyond-5G RIS-assisted mmIDs for future applications, such as smart cities, smart agriculture, and industry 4.0, in complex real-world environments.

REFERENCES

[1] L. S. Vailshery. (Jul. 2023). *IoT Connected Devices Worldwide 2019–2030*. [Online]. Available: https://www.statista.com/statistics/1183457/iot-connected-devices-worldwide/

[2] I. F. Akyildiz, S. Nie, S.-C. Lin, and M. Chandrasekaran, "5G roadmap: 10 key enabling technologies," *Comput. Netw.*, vol. 106, pp. 17–48, Sep. 2016. [Online]. Available: https://www.sciencedirect.com/science/article/pii/S1389128616301918

[3] B. Yang, Z. Yu, J. Lan, R. Zhang, J. Zhou, and W. Hong, "Digital beamforming-based massive MIMO transceiver for 5G millimeter-wave communications," *IEEE Trans. Microw. Theory Techn.*, vol. 66, no. 7, pp. 3403–3418, Jul. 2018.

[4] E. G. Larsson and H. V. Poor, "Joint beamforming and broadcasting in massive MIMO," *IEEE Trans. Wireless Commun.*, vol. 15, no. 4, pp. 3058–3070, Apr. 2016.

[5] E. Basar, "Reconfigurable intelligent surface-based index modulation: A new beyond MIMO paradigm for 6G," *IEEE Trans. Commun.*, vol. 68, no. 5, pp. 3187–3196, May 2020.
[6] M. D. Renzo et al., "Smart radio environments empowered by reconfigurable intelligent surfaces: How it works, state of research, and the road ahead," *IEEE J. Sel. Areas Commun.*, vol. 38, no. 11, pp. 2450–2525, Jul. 2020.
[7] C. Liaskos, S. Nie, A. Tsioliaridou, A. Pitsillides, S. Ioannidis, and I. Akyildiz, "A new wireless communication paradigm through software-controlled metasurfaces," *IEEE Commun. Mag.*, vol. 56, no. 9, pp. 162–169, Sep. 2018.
[8] S. Kayraklık, I. Yildirim, Y. Gevez, E. Basar, and A. Görçin, "Indoor coverage enhancement for RIS-assisted communication systems: Practical measurements and efficient grouping," in *Proc. IEEE Int. Conf. Commun. (ICC)*, Jun. 2023, pp. 485–490.
[9] C. Huang, A. Zappone, G. C. Alexandropoulos, M. Debbah, and C. Yuen, "Reconfigurable intelligent surfaces for energy efficiency in wireless communication," *IEEE Trans. Wireless Commun.*, vol. 18, no. 8, pp. 4157–4170, Aug. 2019.
[10] Y. Liu et al., "Reconfigurable intelligent surfaces: Principles and opportunities," *IEEE Commun. Surveys Tuts.*, vol. 23, no. 3, pp. 1546–1577, 3rd Quart., 2021.
[11] W. Tang et al., "Wireless communications with reconfigurable intelligent surface: Path loss modeling and experimental measurement," *IEEE Trans. Wireless Commun.*, vol. 20, no. 1, pp. 421–439, Jan. 2021.
[12] A. Eid, J. G. D. Hester, and M. M. Tentzeris, "Rotman lens-based wide angular coverage and high-gain semipassive architecture for ultralong range mm-wave RFIDs," *IEEE Antennas Wireless Propag. Lett.*, vol. 19, no. 11, pp. 1943–1947, Nov. 2020.
[13] A. Eid, J. Hester, and M. M. Tentzeris, "A scalable high-gain and large-beamwidth mm-wave harvesting approach for 5G-powered IoT," in *Proc. IEEE MTT-S Int. Microw. Symp.*, Jun. 2019, pp. 1309–1312.
[14] I.-T. Chen, C. A. Lynch, A. Eid, J. G. D. Hester, and M. M. Tentzeris, "Rotman-lens-based reconfigurable intelligence surface mmID with energy harvesting capability," in *IEEE MTT-S Int. Microw. Symp. Dig.*, Jun. 2023, pp. 991–994.
[15] R. Rotman, M. Tur, and L. Yaron, "True time delay in phased arrays," *Proc. IEEE*, vol. 104, no. 3, pp. 504–518, Mar. 2016.

I-Ting Chen (Student Member, IEEE) received the B.S. degree in biomedical engineering from Purdue University, West Lafayette, IN, USA, in 2020. She is currently pursuing the Ph.D. degree in electrical engineering with Georgia Institute of Technology, Atlanta, GA, USA.

She is currently a Research Assistant with the ATHENA Group, Georgia Institute of Technology. Her research interests include energy harvesting/wireless power transfer, reconfigurable intelligence surfaces, and radio frequency identification (RFID). She developed inkjet-printed and highly integrated/multilayer millimeter identification (mmID) for wireless applications.

Ms. Chen received the second place Best Contribution Award in IEEE Wireless Power Technology Conference and Expo (WPTCE) 2023 in San Diego, CA, USA.

Charles A. Lynch III (Student Member, IEEE) received the B.S. degree in electrical engineering from the Rose-Hulman Institute of Technology, Terre Haute, IN, USA, in 2019. He is currently pursuing the M.S. and Ph.D. degrees in electrical engineering with Georgia Institute of Technology, Atlanta, GA, USA.

He is currently a Research Assistant with the ATHENA Group, Georgia Institute of Technology. His current research interests include the design, simulation, and fabrication of RF and millimeter-wave devices, specifically RFIDs and mmIDs and combining these low-power, wearable, ultralow-cost devices with radar for localized sensing in Internet of Things systems.

Mr. Lynch III received the audience choice in the 3MT Competition at the 2023 IEEE IMS conference.

Aline Eid (Member, IEEE) received the M.S. degree in electrical and computer engineering from American University of Beirut, Beirut, Lebanon, in 2017, and the Ph.D. degree in electrical and computer engineering from Georgia Institute of Technology, Atlanta, GA, USA, in Spring 2022.

She is an Assistant Professor with the Department of Electrical and Computer Engineering with the University of Michigan, Ann Arbor, MI, USA. Prior to that, she was a Post-Doctoral Associate with the MIT Media Laboratory, Cambridge, MA, USA. In 2020, she did a six-month internship with Google wearable/augmented reality (AR)/virtual reality (VR) and advanced technology projects (ATAP) groups. She is an inventor of seven patents, and author/co-author of more than 70 conference papers, journal articles, and book chapters. Her vision is to build a responsive and sustainable infrastructure through the development of innovative wireless systems. Her research interests are in wireless sensing, mm-wave backscatter communications, and wireless power transfer.

Prof. Eid was a recipient of the 2020 IEEE MTT-S Graduate Fellowship and Tom Brazil Awards. She is also the recipient of more than 20 awards, fellowships, and grants, including best paper awards at IEEE RFID, IEEE APS, and IEEE WPTCE.

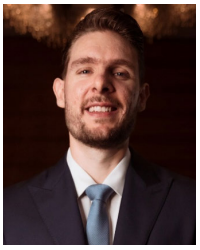

Jimmy G. D. Hester (Member, IEEE) received the M.S. and Ph.D. degrees in electrical and computer engineering from Georgia Institute of Technology, Atlanta, GA, USA, in 2014 and 2019, respectively.

He is now the CTO and Co-Founder of Atheraxon—the developer of the Theia mmWave localization technology—and an Adjunct Professor with the Department EECS, University of Michigan, Ann Arbor, MI, USA. His areas of expertise include backscatter communications, mm-wave antenna design, radar systems design, radar signal processing, digital communications, inkjet printing, and nanomaterial-based sensing.

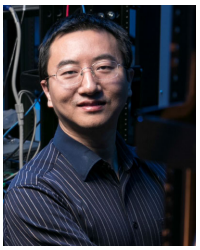

Kai Zeng (Member, IEEE) received the Ph.D. degree in electrical and computer engineering from Worcester Polytechnic Institute (WPI), Worcester, MA, USA, in 2008.

He was a Post-Doctoral Scholar with the Department of Computer Science, University of California at Davis (UCD), Davis, CA, USA, from 2008 to 2011. He was an Assistant Professor, with the Department of Computer and Information Science, University of Michigan-Dearborn, Dearborn, MI, USA, from 2011 to 2014. He is currently a Professor with the Department of Electrical and Computer Engineering and the Department of Computer Science, George Mason University, Fairfax, VA, USA. His current research interests include the security of 5G and FutureG wireless networks, cyber–physical systems/Internet-of-Things security and privacy, machine learning applications in wireless cybersecurity, generative AI security, and spectrum sharing systems security and privacy.

Dr. Zeng was a recipient of U.S. National Science Foundation Faculty Early Career Development (CAREER) Award in 2012. He received the Excellence in Postdoctoral Research Award from UCD in 2011 and the Sigma Xi Outstanding Ph.D. Dissertation Award from WPI in 2008. He has served as an Associate Editor for IEEE TRANSACTIONS ON INFORMATION FORENSICS AND SECURITY, IEEE TRANSACTIONS ON MACHINE LEARNING IN COMMUNICATIONS AND NETWORKING, IEEE TRANSACTIONS ON COGNITIVE COMMUNICATIONS AND NETWORKING, and IEEE TRANSACTIONS ON WIRELESS COMMUNICATIONS.

Manos M. Tentzeris (Fellow, IEEE) received the Diploma degree (magna cum laude) in electrical and computer engineering from the National Technical University of Athens, Athens, Greece, and the M.S. and Ph.D. degrees in electrical engineering and computer science from the University of Michigan, Ann Arbor, MI, USA, in 1993 and 1998, respectively.

He was a Visiting Professor with the Technical University of Munich, Munich, Germany, in 2002; GTRI-Ireland, Athlone, Ireland, in 2009; and LAAS-CNRS, Toulouse, France, in 2010; and a Humboldt Guest Professor with FAU, Nuremberg, Germany, in 2019. He is currently the Ed and Pat Joy Chair Professor with the School of Electrical and Computer Engineering, Georgia Institute of Technology, Atlanta, GA, USA, where he heads the ATHENA Research Group (20 researchers). He was the Head of the GT ECE Electromagnetics Technical Interest Group, Georgia Electronic Design Center Associate Director of RFID/Sensors Research, Georgia Institute of Technology NSF-Packaging Research Center Associate Director of RF research, and the RF Alliance Leader. He has helped develop academic programs in 3-D/inkjet-printed RF electronics and modules, flexible electronics, origami and morphing electromagnetics, highly integrated/multilayer packaging for RF, millimeter-wave, subterahertz, and wireless applications using ceramic and organic flexible materials, paper-based RFIDs and sensors, wireless sensors and biosensors, wearable electronics, "Green" and transient electronics, energy harvesting and wireless power transfer, nanotechnology applications in RF, microwave MEMs, and SOP-integrated (UWB, multiband, mmW, and conformal) antennas. He has authored more than 850 papers in refereed journals and conference proceedings, seven books, and 26 book chapters. He has given more than 150 invited talks to various universities and companies all over the world.

Dr. Tentzeris is a member of the URSI-Commission D and the MTT-15 Committee, an Associate Member of EuMA, a Fellow of the Electromagnetic Academy, and a member of the Technical Chamber of Greece. He was a recipient/co-recipient of the 2024 Georgia Tech Outstanding Achievement in Research Innovation Award, the 2023 Proceedings of IEEE Best Paper Award, the 2022 Georgia Tech Outstanding Doctoral Thesis Advisor Award, the 2021 IEEE Antennas and Propagation Symposium (APS) Best Student Paper Award, the 2019 Humboldt Research Prize, the 2017 Georgia Institute of Technology Outstanding Achievement in Research Program Development Award, the 2016 Bell Labs Award Competition Third Prize, the 2015 IET Microwaves, Antennas, and Propagation Premium Award, the 2014 Georgia Institute of Technology ECE Distinguished Faculty Achievement Award, the 2014 IEEE RFID-TA Best Student Paper Award, the 2013 IET Microwaves, Antennas and Propagation Premium Award, the 2012 FiDiPro Award in Finland, the iCMG Architecture Award of Excellence, the 2010 IEEE Antennas and Propagation Society Piergiorgio L.E. Uslenghi Letters Prize Paper Award, the 2011 International Workshop on Structural Health Monitoring Best Student Paper Award, the 2010 Georgia Institute of Technology Senior Faculty Outstanding Undergraduate Research Mentor Award, the 2009 IEEE Transactions On Components And Packaging Technologies Best Paper Award, the 2009 E. T. S. Walton Award from the Irish Science Foundation, the 2007 IEEE AP-S Symposium Best Student Paper Award, the 2007 IEEE MTT-S IMS Third Best Student Paper Award, the 2007 ISAP Poster Presentation Award, the 2006 IEEE MTT-S Outstanding Young Engineer Award, the 2006 Asia–Pacific Microwave Conference Award, the 2004 IEEE Transactions on Advanced Packaging Commendable Paper Award, the 2003 NASA Godfrey "Art" Anzic Collaborative Distinguished Publication Award, the 2003 IBC International Educator of the Year Award, the 2003 IEEE CPMT Outstanding Young Engineer Award, the 2002 International Conference on Microwave and Millimeter-Wave Technology Best Paper Award, Beijing, China, the 2002 Georgia Institute of Technology–ECE Outstanding Junior Faculty Award, the 2001 ACES Conference Best Paper Award, the 2000 NSF CAREER Award, and the 1997 Best Paper Award of the International Hybrid Microelectronics and Packaging Society. He was the General Co-Chair of the 2023 IEEE WIRELESS POWER TRANSFER TECHNOLOGY CONFERENCE AND EXPO in San Diego and the 2019 IEEE APS Symposium in Atlanta. He was the TPC Chair of the IEEE MTT-S IMS 2008 Symposium and the Chair of the 2005 IEEE CEM-TD Workshop. He is the Vice-Chair of the RF Technical Committee (TC16) of the IEEE CPMT Society. He is the Founder and the Chair of the RFID Technical Committee (TC24) of the IEEE MTT-S and the Secretary/Treasurer of the IEEE C-RFID. He has served as an Associate Editor for IEEE TRANSACTIONS ON MICROWAVE THEORY AND TECHNIQUES, the IEEE TRANSACTIONS ON ADVANCED PACKAGING, and the International Journal on Antennas and Propagation. He is currently one IEEE EPS Distinguished Lecturer and has served as one of IEEE MTT-S Distinguished Microwave Lecturers and as one of IEEE CRFID Distinguished Lecturers.